

Tunable femtosecond electron and X-ray double-beams from a compact laser-driven accelerator

J. Wenz*,^{1,2} K. Khrennikov*,^{1,2} A. Döpp*,^{1,2} M. Gilljohann,^{1,2} H. Ding,^{1,2} J. Götzfried,^{1,2} S. Schindler,^{1,2} A. Buck,^{1,2} J. Xu†,² M. Heigoldt,^{1,2} W. Helml,¹ L. Veisz,^{2,3} and S. Karsch^{1,2}

¹*Ludwig-Maximilians-Universität München, Am Coulombwall 1, 85748 Garching, Germany*

²*Max Planck Institut für Quantenoptik, Hans-Kopfermann-Str. 1, Garching 85748, Germany*

³*Department of Physics, Umea University, SE-901 87 Umea, Sweden*

Ultrafast pump-probe experiments open the possibility to track fundamental material behavior like changes in its electronic configuration in real time.^{1,2} So far, such measurements have widely relied on high harmonic generation (HHG) with ultrashort laser pulses, limiting the achievable wavelength range to the extreme ultraviolet regime³. However, to directly excite site-specific core states of molecules or more complex systems, photon energies in the water window and above are required. Novel light sources based on laser-driven electron accelerators have demonstrated bright radiation production over a wide energy range⁴. Given the phase space of the electron bunches could be shaped in an adequate way, these sources would also be suitable for high-energy ultrafast pump-probe experimentation. Here, we report for the first time on the simultaneous generation of two monoenergetic electron bunches with individually tunable energy up to several hundred MeV. Due to the underlying injection physics, the lengths of the bunches as well as their temporal separation inherently amount to femtoseconds. In combination with established beam-handling and insertion devices, these results pave the way to laboratory-scale multi-beam experiments with unprecedented scope in energy tuning and time resolution.

Understanding the dynamics of materials on the time scale of electronic, atomic and molecular motion is one of the grand challenges of contemporary physics, chemistry and biology. Particularly useful in this regard are pump-probe experiments, in which a process is triggered using a pump pulse and whose temporal evolution is then studied using a probe pulse. Due to the stringent requirements on the durations of both pump and probe in ultrafast science, this kind of measurement has only become available with the advent of ultrashort-pulse laser sources.⁵ Moreover, the properties of the radiation source dictate which type of systems can be studied. While infrared laser pulses can be used to excite or manipulate some electronic and magnetic states, XUV/X-ray photons can, for instance, directly stimulate electronic transitions of core states. Furthermore, X-ray probe beams can provide crucial advantages such as atomic or even chemical selectivity, as well as quantitative information about spin and orbital moments.⁶ But despite substantial

efforts to increase the photon energy available from up-conversion schemes such as HHG in gases⁷, to date no laboratory-scale source can efficiently pump and probe processes at keV-energies and above. Accordingly, the study of ultrafast processes in this regime remains restricted to large-scale installations like the LCLS X-ray Free-Electron Laser⁸. These accelerator-based sources produce X-ray pulses of unrivaled peak-intensity, yet time-resolved studies usually only exploit the temporal structure of the pulses.⁹ Additionally, due to their small number world-wide, access to free-electron lasers is restricted to a few experimental groups per year, and the demand of round-the-clock operation severely limits their flexibility in terms of setup changes between beam times. Thus, it is very difficult to explore new or unconventional experimental configurations or drive novel developments in radiation generation and control. It is therefore highly desirable to establish a versatile laboratory-scale source with ultrashort pump-probe capability in the XUV and X-ray range.

Such a source is within reach thanks to the rapid development of novel, laser-driven accelerators. The electron beams produced by the interaction of an intense ultrashort laser pulse with a plasma are inherently synchronized to the laser and have a femtosecond duration.⁴ While this property alone is already of interest for pump-probe experiments based on ultrafast electron diffraction^{10,11}, the beams can also be used to generate ultrashort pulses of synchrotron-like radiation. Depending on the method to create this radiation, XUV¹², X-ray^{13,14} or γ -ray¹⁵ photons can be generated. Recently, first X-ray absorption spectroscopy measurements in warm-dense matter, using an infrared pump and a keV-range betatron probe beam, showcased the potential of such laser-driven X-ray sources for pump-probe experiments¹⁶. To further extend this capability to high-photon energy pump-probe experiments, the paramount challenge is to generate two monoenergetic electron beams with a tunable delay that can be used to generate spectrally distinct pump and probe pulses.

Over the past decade, a variety of techniques has been introduced to generate narrow bandwidth electron beams using laser wakefield acceleration.¹⁷ Passive injection schemes relying on laser-evolution¹⁸ or self-truncation of the injection process¹⁹ remain the most popular, due to their simplicity to implement in experiment. However, to generate tunable double-beams it is necessary to trigger the electron injection process at controlled positions,

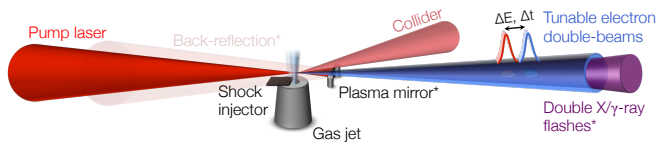


Figure 1: **Double-beam femtosecond electron and X-ray source.** Using a single high-power laser system, two injection events are triggered by shock-front and colliding pulse injection, resulting in the generation of spectrally distinct electron beams with femtosecond delay. In a second experiment, these electrons are used for radiation generation using Compton backscattering following the reflection of the pump laser on a plasma mirror.

which is not possible using these methods. Instead, experimentally more challenging active electron injection techniques are required, among which optical injection²⁰ and shock-front injection²¹ are arguably the most promising methods. The former adds a second collider pulse to the setup to create favorable trapping conditions during the interaction with the drive pulse²⁰. While injection may be caused by several different mechanisms^{22–24}, depending on the exact conditions, all variants of optical injection produce ultrashort, quasi-monoenergetic electron bunches, whose energy can be adjusted by moving the collision point along the plasma channel. Shock-front injection²⁵ is an injection method purely based on plasma density tailoring that uses a sharp blade or wafer to create a supersonic shock in the gas flow of the target. At this shock front, a rapid transition from high plasma density (n_0) to low density (n_1) occurs, which leads to a sudden increase of the plasma wavelength λ_p . Accordingly, the laser wakefield expands, which temporarily facilitates trapping of electrons. As for colliding pulse injection, the injection position is tunable; in this case by moving the blade with respect to the gas jet.

We have compared both techniques in experiments with the ATLAS Ti:Sa laser system, using de Laval gas nozzles to create a supersonic gas flow suitable for shock-front injection (cf. Methods and Figure 1). Figure 2 shows the spectra of electron beams obtained using both shock-front and colliding pulse injection techniques separately, albeit with the same driving laser, focusing geometry, gas nozzle and gas density. The beams exhibit similar properties and have, for a laser-wakefield accelerator, a high stability, reproducibility and tuning range³⁷. The use of the shock-front injector results in a higher spectral charge density compared to the optical scheme, which is, however, paired with a slightly increased energy bandwidth.

Since the acceleration length is well below the dephasing length³⁸, the energy gain scales linearly with the acceleration distance, and the acceleration gradient can be determined for both schemes. We find that the average acceleration experienced by shock-injected beams is 74 ± 6 GeV/m, while we measure 60 ± 12 GeV/m for optically injected beams. The difference between gradi-

ent measurements seems to be caused by beam-loading effects, because the beam charge is not constant over the scan and electron bunches do not necessarily have the same charge density. The beam-loading effects are manifested by the diminishing bunch charge and hence higher energy when the blade is close to the gas jet entrance (where n_0/n_1 is smaller in the case of shock-front injection). In contrast, the beam charge for colliding pulse injection increases towards the beginning of the jet, which is expected to lower the final beam energy. Here, the beam charge is related to the product of the vector potentials of collider and main beam²⁶, so the increasing charge is likely a result of the relative focusing between the two lasers. For both measurements the divergence of the electrons beams scales as theoretically expected with $\gamma^{3/4}$, where γ is the relativistic factor of the electron beam²⁷.

In a next step, we integrated both injection configurations into the same setup, which allowed us to use them simultaneously. As moving the shock front perturbs the beginning of the gas jet, we moved the blade to a fixed position which continuously results in a peak energy of about 40 MeV. Then, the colliding pulse is activated and the entire jet (including the blade which forms the shock) is moved along the laser axis with respect to the collision position. Accordingly, the relative position

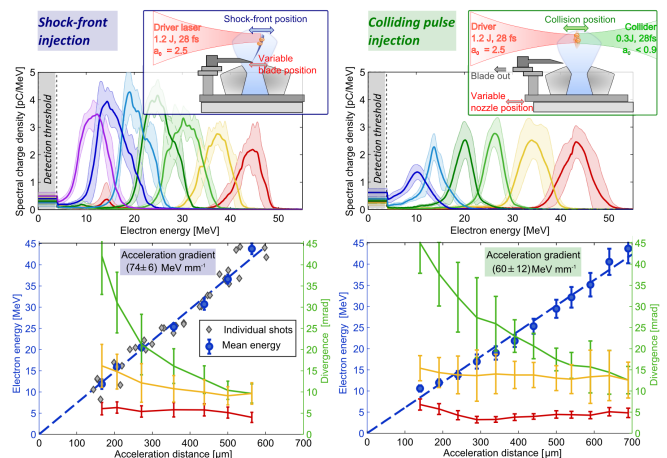


Figure 2: **Experimental tuning of electron beam energy using shock-front (left) and colliding pulse injection schemes (right).** Inset: Sketch of the basic setup. Tuning of the electron energy is obtained by variation of the acceleration length by adjusting the position of the blade (left) or collision position (right) within the gas flow. *Top:* Averaged energy spectra of selected 10 shots for different acceleration length settings. *Bottom:* Resulting beam characteristics. Blue dots represent the averaged peak energy of the bunch, with error bars showing the rms stability over the complete scan. Red curves depict the average spectral widths (FWHM) for each energy setting. Green (yellow) curves show the (normalized by $\gamma^{3/4}$, see main text) beam divergence. Energy spectra of individual shots of the whole experimental run can be found in the supplementary material.

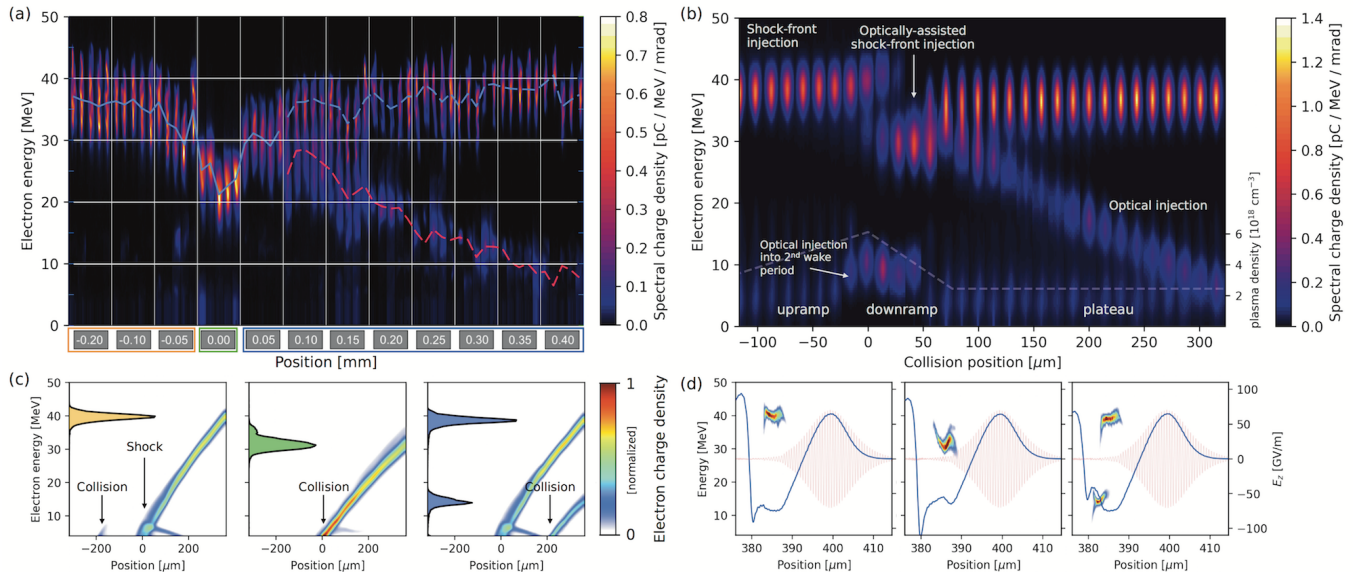


Figure 3: Demonstration of double-beam injection and particle-in-cell simulations. (a) Individual electron spectra for different settings of the optical collision position and fixed shock-front. Positions are normalized to the shock-front. For negative collision position settings, i.e., in the density upramp, no optically injected electrons are observed. Collision at 0 mm shows enhanced injection, while the peak energy (blue line) is reduced due to beam-loading. At positive values: Demonstration of the tunable optically injected beam behind the leading electron beam from the shock-front injection scheme (peak energy shown as red line). (b) PIC simulations of the experiment, clearly showing the same three distinct regimes for collision in the upramp, downramp and on the plateau. (c) Energy evolution in the first bubble for the three cases. For a collision in the upramp electrons are initially accelerated, but are quickly lost due to the super-luminal phase velocity of the wake. If the collision occurs during the downramp, the amount of injected charge increases, and for collision on the plateau two separate beams emerge. (d) Longitudinal phase space (false color), on-axis plasma field lineouts (blue) and laser field (red) at the end of the accelerator for each case.

of shock and pulse collision can be adjusted.

In doing so, we observe three distinct behaviors, cf. Figure 3a. When the collision occurs before the shock, the electron beam spectra show only a single monoenergetic peak. This signal is indistinguishable from sole shock-front injection, indicating that the optical injection mechanism is suppressed. With the collision occurring close to the density transition, we observe that the energy of the mono-energetic feature suddenly decreases. As this effect is accompanied by an increased beam charge, it suggests that both injection methods assist each other and cause beam loading. Then, as we move the collision point further outwards onto the density plateau, two separate monoenergetic peaks form. The first is at an energy very similar to shock-front injection without the collision pulse active and is therefore still attributed to shock-front injection. The second, lower energy peak could be adjusted between 10 – 25 MeV by varying the collision position and is hence the result of colliding pulse injection.

To understand the physics underlying the different operation regimes of the injector, we have performed a series of quasi-3D particle-in-cell simulations. The results, which are depicted in Figure 3b-d, accurately reproduce the experimentally observed behavior. Before

the shock, the plasma density is increasing and hence, the plasma wavelength decreases. Analogous to the plasma wave expansion during shock-front injection, this causes a wake contraction at a velocity $v_{ramp} \propto d\lambda_p/dt$. Electron injection and acceleration only occurs if the electrons can reach a velocity close to the wake’s phase velocity $v_\phi \simeq v_g - v_{ramp}$, where v_g is the group velocity of the laser. During the upramp ($v_{ramp} < 0$), the phase velocity is increased and can even reach superluminal speed²⁸. So despite electrons gaining momentum after the pulse collision, injection is inhibited during this phase. The situation changes close to the density peak of the shock, where the relaxed injection conditions allow the pre-accelerated electrons to get trapped in the second wakefield period.

Once the pulse collision occurs at the density downramp, the injection behavior changes. A single injection event is observed, with increased charge and lower final beam energy. Simulations suggest that we are operating in the regime of optical transverse injection, where the pulse collision causes a rapid contraction and re-expansion of the wakefield²⁴. Accordingly, this regime can be understood as optically-assisted shock-front injection. As this combined injection occurs inside the same plasma cavity, the increased charge causes beam-loading and thus, lowers the energy gain.

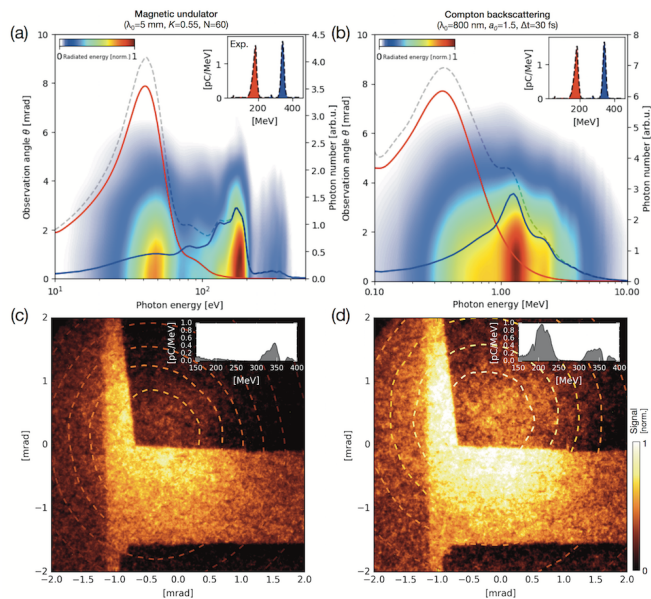


Figure 4: **Radiation generation.** (a-b) Simulations of synchrotron radiation based on a measured electron beam spectrum (inset) for a magnetic undulator (a) and an all-optical Compton source (b). Red (low energy) and blue (high energy) lines show the on-axis photon number originating from the respective electron bunches. Colormaps in both plots show the angularly resolved radiation emission. (c-d) Observed radiation signal from Compton backscattering (10 shot average) for a single electron bunch (c) and a double bunch (d). The average electron spectra are shown as insets. Contour lines show simulated intensity profiles for the same electron beams and a colliding beam with $a_0 = 1.5$. Darker areas are covered with transmission filters.

Moving the collision point towards the end of the jet, the two injection events separate, resulting in two distinct peaks in the spectrum. The temporal delay of both bunches is determined by the amount of dephasing occurring between the injection events, leading to a robust temporal synchronization. For a distance Δx between shock and collision, the ultrashort bunch delay can be estimated as

$$(1 - v_g/c_0) \cdot \Delta x/c_0 \simeq 2 \text{ fs} \cdot n_e [10^{18} \text{ cm}^{-3}] \cdot \Delta x [\text{mm}].$$

Note that this is likely to slightly overestimate the delay, because optical transverse injection does not strictly occur at the rear side of the bubble. The experimental data also showed that beam charge and energy are reduced compared to pure colliding pulse injection. This is a signature of the beam-loading caused by the first, shock-injected beam in proximity to the optically injected beam and can be clearly observed in the shape of the simulated longitudinal wakefields (cf. Fig.3d).

Ultrashort MeV-scale electron beams are either of immediate interest for measurements based on femtosecond electron diffraction or they can be coupled to insertion devices to generate secondary radiation. However, depending on the desired wavelengths, this can require higher electron beam energies. We have therefore re-

peated the experiment using an upgraded laser and larger gas jets, which allowed us to increase the electron energy by almost an order of magnitude: Electrons from shock-front injection routinely reached 350 MeV, while the energy of the optically injected beam was tuned from 50 to 200 MeV. Simulations show that the electron beams accelerated in the new experiment are suitable to generate XUV radiation (using magnetic undulators, Fig.4a) or even γ -rays (based on Compton backscattering, Fig.4b). Importantly, the radiation from both electron bunches is spectrally distinguishable and has a predefined temporal structure, with the high energy pulse coming first, followed by the low energy pulse. Given the longer acceleration length in this experiment, the range to directly adjust the temporal delay between both bunches is also wider (~ 20 fs). Even greater tunability could be achieved by using a magnetic chicane, which would allow to adjust the pulse delay on both femtosecond to picosecond scales. Note that the final pulse duration would be determined by the energy spread of each bunch in this case.

As a proof-of-principle experiment, we have performed Compton backscattering with both single and double bunch electron beams. For this, we integrated a plasma mirror into the experimental setup that retro-reflects the drive laser pulse of the wakefield accelerator onto the trailing electrons.²⁹ The upper edge of the plasma mirror is placed close to the laser axis, allowing the colliding beam to pass over it. Using only shock-front injection (peak at 350 MeV, 35.5 pC total charge), we observe a 2.3 mrad FWHM photon beam on the detector. Activating the collision pulse added a quasi-monochromatic bunch at 210 MeV with 44.5 pC charge to the electron beam. Under these conditions the peak signal on the scintillator is 45 % higher and the beam divergence increased to 2.8 mrad. Simulations based on the measured electron beams predict a similar signal gain (57%) and reproduce the beam profile (see contour lines in Fig.4c-d). While the setup was not suitable to measure the duration of the photon beam, the temporal structure of the backscattered radiation will be determined by the electron beam⁴. Based on the simulations and experimental measurements of the electron bunch duration^{28,30}, it is therefore expected that the emitted radiation consisted of two delayed femtosecond bursts.

In conclusion, we have for the first time demonstrated monoenergetic femtosecond electron double-beams with tunable energy and delay. The double bunch structure was successfully produced at peak energies of 40 and 350 MeV, and we demonstrated the generation of femtosecond radiation using an all-optical Compton source. Our analysis showed the complex interplay of two different electron injection schemes and we identified regimes for double-beam generation as well as a new regime of optically-assisted shock-front injection. Further studies may also allow generating specific longitudinal charge density profiles to optimize the accelerator performance or study advanced wakefield acceleration schemes. Most

importantly, we suggest to combine either conventional or optical undulators with the laser wakefield accelerator to generate radiation in the XUV, X-ray and γ -ray range. In this way, the presented source paves the way to study a large variety of ultrafast phenomena on a laboratory scale, providing two electron beams and double pulses of femtosecond secondary radiation with inherent synchronization to the driving laser system. It therefore uniquely combines multiple, individually tunable ultra-short radiation pulses for both pump and probe into a common and compact setup.

Methods

Laser systems. The first series of experiments demonstrating low-energy electrons (< 50 MeV) were performed using the ATLAS Ti:Sapphire laser at the MPI for Quantum Optics (MPQ), which delivered 1.6 J energy within 28 fs duration (60 TW) laser pulses, centered at 800 nm wavelength. The main part of the laser (1.2 J) has been focused with an F/13 off-axis parabolic mirror reaching intensity of 1.3×10^{19} W/cm² ($a_0 = 2.5$) in a focal spot of $11 \times 12 \mu\text{m}^2 \sim 1.5$ mm above the nozzle exit. For colliding pulse injection, a small part of beam containing ~ 0.3 J has been cut off by a pick-up mirror in the experimental chamber and was focused by an F/26 off-axis parabolic mirror. For perfect beam overlap, this would result in a peak potential of up to $a_1 \simeq 0.9$. However, the actual intensity during the pulse interaction is expected to be much lower, because during alignment we do not optimize towards highest overlap (as in experiments on Thomson-Backscattering¹⁴), but for best energy spread and stability of the optically-injected electron bunch.

High energy experiments have been carried out with the upgraded ATLAS laser system, situated at the Laboratory for Extreme Photonics (LEX) at Ludwig-Maximilians University of Munich (LMU), which delivered up to 2.5 J pulses of similar duration. The pulses were focused on the gas target in a f/25 geometry to a peak intensity of 5.5×10^{18} W/cm², while the colliding pulse had the same parameters as in the first experiment.

Gas targets and diagnostics. In the first experiments, the gas target was a 300 micrometer supersonic gas nozzle of de Laval geometry. The shock-front was realized by introducing a razor blade perpendicular to the gas flow (see Figure 1). In the second experiment, a larger 5 mm nozzle was used in conjunction with an adjustable silicon wafer. The density profile is characterized using both few-cycle microscopy and interferometry. The electron energy was characterized using dipole magnet spectrometers. During the first experiment a magnet spectrometer consisting of a 0.91 T permanent magnet, resolving electron energies from 2.5 to 400 MeV³¹. In the second experiment, an 80 cm permanent magnet (0.85 T) was used, measuring electron energies from 50 MeV onwards. Radiation emission in the Compton backscat-

tering experiment was detected using a Gd₂O₂S:Tb scintillator, which is fiber-coupled to an MCP-based image intensifier and whose amplified signal is coupled to a CCD sensor³².

Particle-in-cell simulations. The simulations were performed with the quasi-3D code CALDER-CIRC³³, using the two modes $m=0$ and $m=1$ for modeling of the laser and wakefield. The resolution chosen for the parameter scan was $\Delta x = 0.25k_0^{-1}$, $\Delta r = 1.0k_0^{-1}$ and 40 particles per cell ($k_0^{-1} = \lambda_0/2\pi \simeq 127$ nm). The laser driver is initialized with a peak potential $a_0 = 2.5$ and a spot size of $12 \mu\text{m}$, whereas the collider has an intensity $a_1 = 0.3$. As the density transition length was not directly measured in the first experiment, a plasma gradient length similar to Swanson et al.³⁴ was chosen ($75 \mu\text{m} \sim 3.5\lambda_p$). A total of 40 PIC simulations was performed for the parameter scan shown in Fig.3. We note that some experiments suggest an even shorter transition length²⁸. For this case, simulations still show the same three regimes of operation, but the final energy spread is higher because of accumulated energy chirp at the end of the simulation.

Radiation modeling. Synchrotron radiation was calculated using CHIMERA³⁵. For this, the measured electron spectra were modeled using 10^4 test particles, assuming an FWHM beam divergence of 1 mrad. For undulator simulations, the parameters from Fuchs et al. were used, i.e. $K = 0.55$, $N = 60$ and $\lambda_u = 5$ mm. As the exact experimental parameters of the $\lambda_0 = 800$ nm scattering pulse for the all-optical Compton source could not be measured in our setup, we used PIC simulations to estimate the normalized peak potential at the end of the gas target ($a_0 \sim 2$). Taking into account the reflectance of the plasma mirror (~ 0.5), we chose $a_0 = 1.5$ as estimation for the scattering parameter. The duration is assumed as 30 fs FWHM. To generate the simulated beam profiles, the average electron spectra of 10 shots each were used to calculate the energy-dependent far-field emission. In this case, a divergence of 1.5 mrad was used for the low-energy beam and the detector was modeled based on its quantum efficiency.

Acknowledgements

This work was supported by DFG through the Cluster of Excellence Munich-Centre for Advanced Photonics (MAP EXC 158), DFG-Project Transregio TR-18 funding schemes, by EURATOM-IPP and the Max-Planck-Society. L. V. acknowledges the support by a grant from the Swedish Research Council (2016-05409). The authors thank F. Krausz for helpful comments. A.D. thanks I. Andriyash for support with CHIMERA.

Author contributions

*These authors contributed equally to this work. A.B., M.H., K.K., J.W., J.X., L.W. and S.K. performed the

experiments with ATLAS-60 at the MPQ. A.D., H.D., M.G., J.G., S.S. and S.K. performed the experiments with the upgraded laser system at LEX Photonics. A.D., K.K. and J.W. analyzed the experimental data. A.D. performed PIC simulations and radiation calculations. A.D., W.H., K.K., J.W., L.V. and S.K. discussed the results. A.D., K.K. and J.W. wrote the paper. S.K. supervised the project.

[†] J.X. is presently at State Key Laboratory of High Field Laser Physics, Shanghai Institute of Optics and Fine Mechanics, Chinese Academy of Sciences, P. O. Box 800-211, Shanghai 201800, China.

- ¹ A. Rousse, C. Rischel, and J. C. Gauthier, *Reviews of Modern Physics* **73**, 17 (2001).
- ² F. Krausz and M. Ivanov, *Reviews of Modern Physics* **81**, 163 (2009).
- ³ C. Winterfeldt, C. Spielmann, and G. Gerber, *Reviews of Modern Physics* **80**, 117 (2008).
- ⁴ S. Corde, K. Ta Phuoc, G. Lambert, R. Fitour, V. Malka, A. Rousse, A. Beck, and E. Lefebvre, *Reviews of Modern Physics* **85**, 1 (2013).
- ⁵ T. Brabec and F. Krausz, *Reviews of Modern Physics* **72**, 545 (2000).
- ⁶ A. Kirilyuk, A. V. Kimel, and T. Rasing, *Reviews of Modern Physics* **82**, 2731 (2010).
- ⁷ T. Popmintchev, M. C. Chen, D. Popmintchev, P. Arpin, S. Brown, S. Alisauskas, G. Andriukaitis, T. Balciunas, O. D. Mucke, A. Pugzlys, et al., *Science* **336**, 1287 (2012).
- ⁸ P. Emma, R. Akre, J. Arthur, R. Bionta, C. Bostedt, J. Bozek, A. Brachmann, P. Bucksbaum, R. Coffee, F. J. Decker, et al., *Nature Photonics* **4**, 641 (2010).
- ⁹ C. Bostedt, S. Boutet, D. M. Fritz, Z. Huang, H. J. Lee, H. T. Lemke, A. Robert, W. F. Schlotter, J. J. Turner, and G. J. Williams, *Reviews of Modern Physics* **88**, 207 (2016).
- ¹⁰ G. Sciaini and R. J. D. Miller, *Reports on Progress in Physics* **74**, 096101 (2011).
- ¹¹ Z. H. He, B. Beaupaire, J. A. Nees, G. Gallé, S. A. Scott, J. R. S. Pérez, M. G. Lagally, K. Krushelnick, A. G. R. Thomas, and J. Faure, *Scientific Reports* pp. 1–8 (2016).
- ¹² M. Fuchs, R. Weingartner, A. Popp, Z. Major, S. Becker, J. Osterhoff, I. Cortrie, B. Zeitler, R. Horlein, G. D. Tsakiris, et al., *Nature Physics* **5**, 826 (2009).
- ¹³ A. Döpp, B. Mahieu, A. Lifschitz, C. Thauy, A. Doche, E. Guillaume, G. Grittani, O. Lundh, M. Hansson, J. Gautier, et al., *Light: Science & Applications* **6**, e17086 (2017).
- ¹⁴ K. Khrennikov, J. Wenz, A. Buck, J. Xu, M. Heigoldt, L. Veisz, and S. Karsch, *Physical Review Letters* **114**, 195003 (2015).
- ¹⁵ W. Yan, C. Fruhling, G. Golovin, D. Haden, J. Luo, P. Zhang, B. Zhao, J. Zhang, C. Liu, M. Chen, et al., *Nature Photonics* **11**, 514 (2017).
- ¹⁶ B. Mahieu, N. Jourdain, K. Ta Phuoc, F. Dorchies, J. P. Goddet, A. Lifschitz, P. Renaudin, and L. Lecherbourg, *arXiv* pp. 1–6 (2017).
- ¹⁷ V. Malka, *Physics of Plasmas* **19**, 055501 (2012).
- ¹⁸ S. Corde, A. Lifschitz, G. Lambert, K. T. Phuoc, X. Davoine, R. Lehe, D. Douillet, A. Rousse, V. Malka, and C. Thauy, *Nature Communications* **4**, 1501 (2013).
- ¹⁹ M. Mirzaie, S. Li, M. Zeng, N. A. M. Hafz, M. Chen, G. Y. Li, Q. J. Zhu, H. Liao, T. Sokollik, F. Liu, et al., *Scientific Reports* pp. 1–9 (2015).
- ²⁰ J. Faure, C. Rechatin, A. Norlin, A. Lifschitz, Y. Glinec, and V. Malka, *Nature* **444**, 737 (2006).
- ²¹ A. Buck, J. Wenz, J. Xu, K. Khrennikov, K. Schmid, M. Heigoldt, J. M. Mikhailova, M. Geissler, B. Shen, F. Krausz, et al., *Physical Review Letters* **110**, 185006 (2013).
- ²² G. Fubiani, E. Esarey, C. B. Schroeder, and W. P. Lee-mans, *Physical Review E* **70**, 016402 (2004).
- ²³ X. Davoine, E. Lefebvre, C. Rechatin, J. Faure, and V. Malka, *Physical Review Letters* **102**, 065001 (2009).
- ²⁴ R. Lehe, A. F. Lifschitz, X. Davoine, C. Thauy, and V. Malka, *Physical Review Letters* **111**, 085005 (2013).
- ²⁵ K. Schmid, A. Buck, C. M. S. Sears, J. M. Mikhailova, R. Tautz, D. Herrmann, M. Geissler, F. Krausz, and L. Veisz, *Physical Review Special Topics-Accelerators and Beams* **13**, 091301 (2010).
- ²⁶ C. Rechatin, J. Faure, A. Ben-Ismaïl, J. Lim, R. Fitour, A. Specka, H. Videau, A. Tafzi, F. Burgy, and V. Malka, *Physical Review Letters* **102**, 164801 (2009).
- ²⁷ A. G. R. Thomas, *Physics of Plasmas* **17**, 056798 (2010).
- ²⁸ J. Xu, A. Buck, S. W. Chou, K. Schmid, B. Shen, T. Tajima, M. C. Kaluza, and L. Veisz, *Physics of Plasmas* **24**, 083106 (2017).
- ²⁹ K. Ta Phuoc, S. Corde, C. Thauy, V. Malka, A. Tafzi, J. P. Goddet, R. C. Shah, S. Sebban, and A. Rousse, *Nature Photonics* **6**, 308 (2012).
- ³⁰ O. Lundh, J. Lim, C. Rechatin, L. Ammoura, A. Ben-Ismaïl, X. Davoine, G. Gallot, J. P. Goddet, E. Lefebvre, V. Malka, et al., *Nature Physics* **7**, 219 (2011).
- ³¹ C. M. S. Sears, S. B. Cuevas, U. Schramm, K. Schmid, A. Buck, D. Habs, F. Krausz, and L. Veisz, *Review of Scientific Instruments* **81**, 073304 (2010).
- ³² J. Götzfried, A. Döpp, M. Gilljohann, H. Ding, S. Schindler, J. Wenz, L. Hehn, F. Pfeiffer, and S. Karsch, *Nuclear Inst. and Methods in Physics Research, A* pp. 1–4 (2018).
- ³³ A. Lifschitz, X. Davoine, E. Lefebvre, J. Faure, C. Rechatin, and V. Malka, *Journal of Computational Physics* **228**, 1803 (2009).
- ³⁴ K. K. Swanson, H. E. Tsai, S. K. Barber, R. Lehe, H. S. Mao, S. Steinke, J. van Tilborg, K. Nakamura, C. G. R. Geddes, C. B. Schroeder, et al., *Physical Review Accelerators and Beams* **20**, 051301 (2017).
- ³⁵ I. A. Andriyash, R. Lehe, and V. Malka, *Journal of Computational Physics* **282**, 397 (2015).
- ³⁶ W. Lu, M. Tzoufras, C. Joshi, F. Tsung, W. Mori, J. Vieira, R. Fonseca, and L. Silva, *Physical Review Special Topics-Accelerators and Beams* **10**, 061301 (2007).
- ³⁷ See supplementary figure 1 for single shot energy spectra.
- ³⁸ A desphasing length of $L_d \simeq 5$ mm is estimated using the scalings from Lu et al.³⁶ ($a_0 = 2.5$, $n_e = 2.5 \times 10^{18}$ cm⁻³).

Supplementary Material

Characterization of shock front injection and colliding pulse injection

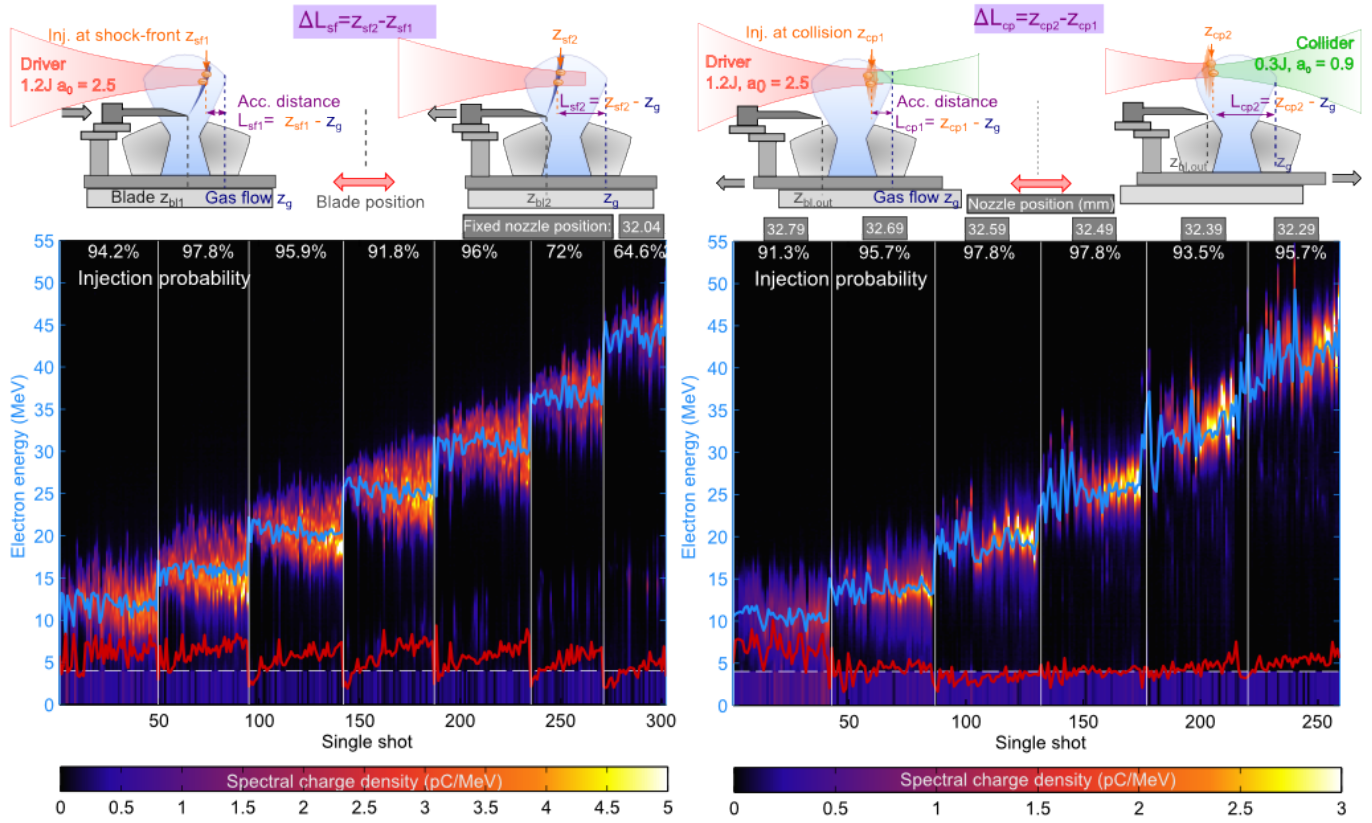


Figure 5: **Single shot electron energy spectra in the shock-front injection (left) vs colliding pulse injection scheme (right).** Left: For the shock-front injection scheme the nozzle position with respect to laser focus was fixed (32.04 mm). Movement of the blade and thus the shock-front position within the gas jet has been varied to adjust the effective acceleration length $L_{acc,sf}$. For the colliding pulse injection the longitudinal laser beam overlap position has been fixed, whereas the nozzle position has been scanned a range of 0.5 mm. The relative position of the laser overlap within the gas jet then determined the acceleration length $L_{acc,cp}$. The single shot electron spectra are presented in false color together with the mean electron energy in blue and the FWHM values of the energy spread in red. For each setting in both schemes, the shots are sorted according to the injected charge.

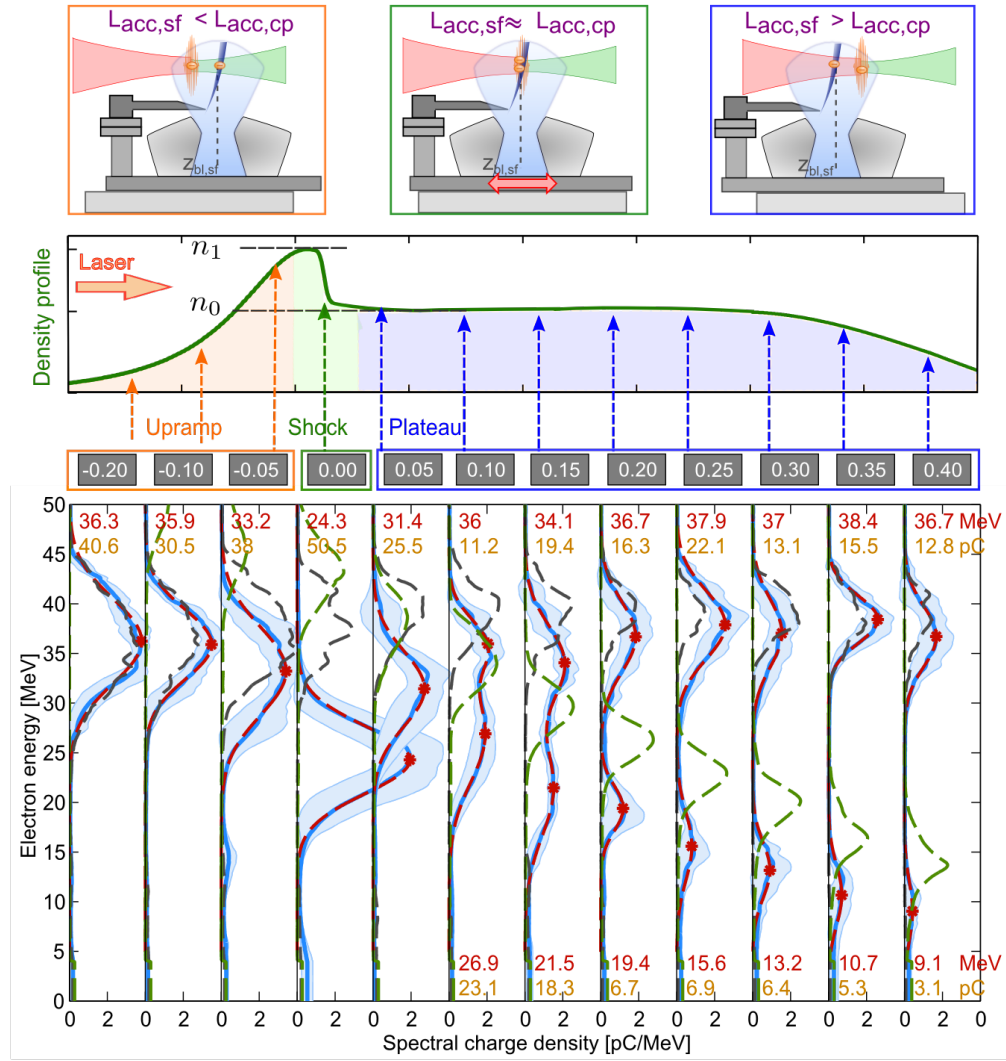


Figure 6: **Lineouts of the averaged integrated electron energy spectra for double-beam injection.** Lineouts (solid blue line) with their reference spectra (dashed lines) obtained with respective injection schemes alone. The peak energy and charge values are obtained from a bi-Gaussian fit (red curve).